



Cite this: DOI: 10.1039/d5ce00068h

Acoustic microscopy study on elasto-mechanical properties of $\text{Lu}_3\text{Al}_5\text{O}_{12}:\text{Ce}$ single crystalline films

 Anton Markovskiy, ^{*ab} Michał Rosiak, ^c Vitalii Gorbenko, ^a Alexander Fedorov, ^d Mieczysław Ciezko, ^c Zbigniew Szczepański, ^c Yuriy Zorenko, ^{*a} Mariusz Kaczmarek, ^c Jerzy Litniewski ^e and Michał Pakuła ^{*c}

This article presents experimental, theoretical, and numerical studies of the propagation of guided ultrasonic waves in a layered epitaxial structure of garnet compounds. A microscopic model, which yields dispersion equations based on material and geometrical properties, is developed. Acoustic microscopy experiments on a YAG:Ce crystal substrate and an epitaxial structure containing LuAG:Ce single crystalline films, grown using the liquid phase epitaxy growth method onto a YAG:Ce crystal substrate, reveal distinct phase velocity behaviors. The YAG substrate exhibits consistent velocities, minimally influenced by frequency, while the epitaxial structure shows dispersion, indicating frequency-dependent phase velocities. Experimental results are compared with numerically calculated dispersion curves, showing high agreement in the low-frequency range and minor deviations at higher frequencies. An optimization procedure is developed and applied, starting with the YAG substrate and extending to the LuAG:Ce film/YAG:Ce crystal epitaxial structure. The procedure allows for the extraction of material properties, offering valuable insights into the mechanical characteristics of the all-solid-state LuAG:Ce film/YAG:Ce crystal structure. This research represents a significant advancement in understanding ultrasonic wave dynamics in layered structures, particularly unveiling previously unexplored elastic properties of LuAG:Ce single crystalline films as a well-known scintillation material.

 Received 17th January 2025,
 Accepted 4th March 2025

DOI: 10.1039/d5ce00068h

rsc.li/crystengcomm

1. Introduction

Garnet crystals, valued for their optical and scintillation properties, play a key role in scientific research and engineering of different types of detectors for monitoring various types of ionization radiations.^{1–6} In recent decades, there has been a notable interest in the LuAG ($\text{Lu}_3\text{Al}_5\text{O}_{12}$) garnet, attributed to its remarkable attributes including high shock resistivity and exceptional chemical, thermal, and radiation stability. Primarily recognized for its efficacy as a heavy, high-response scintillator, Ce^{3+} and Pr^{3+} doped LuAG garnets exhibit fast and efficient luminescence due to the 5d–4f radiation transitions of activators, yielding a high light output upon excitation by various forms of ionizing

radiation.^{7,8} In addition to bulk crystal production through conventional methods such as the Czochralski or modified Bridgman techniques^{7,9} and the fabrication of transparent ceramics *via* various solid-state reaction pathways,^{10–12} single crystalline film (SCF) scintillators based on the LuAG:Ce garnet have been developed using liquid phase epitaxy (LPE)^{6,7} and pulse laser deposition (PLD) growth methodologies.¹³ These thin film scintillators, typically several micrometers thick, demonstrate suitability as heavy screens for X-ray image visualization, even enabling submicron spatial resolution in micrographic devices utilizing conventional X-ray sources and synchrotron radiation.^{14–17} Moreover, the LuAG:Ce garnet stands out as a superbly temperature-stable green phosphor suitable for white LED lighting. Additionally, the quenching temperature for Ce^{3+} within the LuAG host is notably high, starting above 700 K due to the relatively wide energy band gap of this garnet being equal to 8.0 eV at room temperature (RT). However, notable variations of LuAG properties exist depending on the material structure, such as bulk crystals, SCFs, ceramics, or powders.¹⁸

The fundamental premise of the LPE method is to induce supersaturation within the growth solution contained in a liquid flux. This enables the growth process

^a Faculty of Physics, Kazimierz Wielki University, Powst. Wielkopolskich str., 2, 85-090, Bydgoszcz, Poland

^b Lukaszewicz Research Network – Institute of Microelectronics and Photonics, Aleja Lotników 32/46, 02-668, Warsaw, Poland.

E-mail: anton.markovskiy@imif.lukasiewicz.gov.pl

^c Faculty of Mechatronic, Kazimierz Wielki University in Bydgoszcz, Kopernika, 1, 85-074, Bydgoszcz, Poland

^d SSI Institute for Single Crystals, National Academy of Sciences of Ukraine, av. Nauki 60, 61178 Kharkiv, Ukraine

^e Institute of Fundamental Technological Research Polish Academy of Sciences, Pawińskiego 5B, 02-106, Warsaw, Poland

to be conducted at relatively low temperatures, typically around 1000 °C (ref. 19). LuAG:Ce SCFs are typically synthesized using the LPE method from melt-solutions based on the PbO–BaO flux at significantly reduced temperatures, and exhibit a truly stoichiometric content and excellent structural quality compared to their bulk crystal counterparts. Additionally, they demonstrate a lower concentration of main type intrinsic defects of garnet compounds such as Lu_{Al} antisite defects and oxygen vacancies typical for their crystal analog, grown from the melt at high (~2000 °C) temperature in an oxygen-free (Ar) atmosphere.

This paper focuses on the important role of measuring elastic properties in understanding the mechanical interactions of both bulk garnet crystals and thin SCFs grown by the LPE method. The adaptability of the LPE method allows for the precise adjustment of the properties of garnet compounds in the form of films, expanding the possibilities of their use in the design of optoelectronics devices. Central to this exploration is the careful measurement of elastic properties, with techniques like acoustic microscopy playing a key role in understanding the elastic properties of single crystals and SCFs. Insights into elasticity offer information on structural integrity, response to external stimuli, and potential applications in different optoelectronics devices. The measured elastic properties, particularly for unconventional compositions, show promise in discovering materials customized for specific uses.^{20–22}

However, this poses a significant challenge, as the conventional bulk wave theory may not be applicable in this context. Elastic waves in plates or epitaxial layered structures are guided, and in theory, the interpretation of the elasticity of layered structures should employ the guided wave model.^{23,24} Guided waves exhibit dispersion, meaning that the phase velocities vary with frequencies. The elastic properties of the epitaxially grown film can be obtained by fitting the experimentally measured dispersion relation with a theoretical model. An experimental method for measuring wave velocities at different frequencies in layered systems, where the thickness is comparable to the wavelength, involves employing techniques such as acoustic microscopy or ultrasound imaging.^{25,26} These methods enable the precise determination of wave velocities within the layered structure, allowing for a comprehensive analysis of the mechanical properties.^{27–29}

2. Materials

The LuAG:Ce SCF/YAG:Ce SC epitaxial composite structures were prepared at the Chair for Optoelectronic Material of the Faculty of Physics of Kazimierz Wielki University in Bydgoszcz, Poland. Namely, the LPE growth of LuAG:Ce SCFs was performed onto Czochralski grown [111] oriented YAG:Ce crystal substrates, specially prepared by chemical–mechanical polishing in the Institute for Single Crystals, Kharkiv, Ukraine. The film growth was performed in a Pt

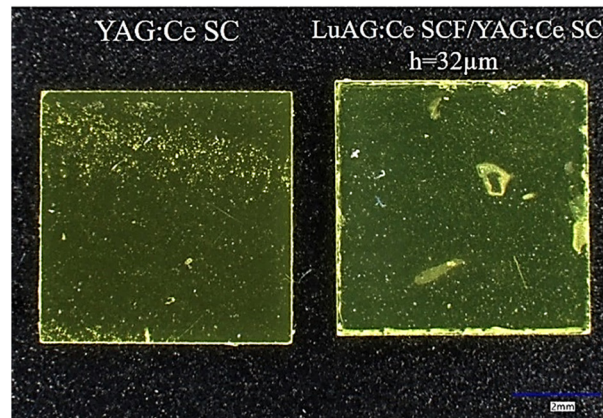


Fig. 1 Photos of the YAG:Ce crystal substrate and LPE grown LuAG:Ce SCF onto a YAG:Ce crystal substrate. The film thickness is conveniently specified for one side of the composite converter, and it's important to highlight that the film maintains uniform thickness on the opposite side of the substrate.

crucible from the supercooled melt solution based on PbO–B₂O₃ (12:1 mole/mole) flux and 4 N purity garnet-forming oxides: Lu₂O₃, Al₂O₃, and CeO₂. The content of garnet components was stoichiometric, calculated regarding the flux composition, see [Materials, 2022] for details.³⁰ Throughout the film growth process, the substrate, horizontally attached to the platinum holder, was rotating at 60–80 rpm in the melt solution. The SCF growth temperature T_g was in the 950–1025 °C range. Under the described conditions, the growth rate was in the $f_s = 0.35$ – $1.6 \mu\text{m min}^{-1}$ range. Fig. 1 presents the photos of the samples of the YAG:Ce crystal substrate and LPE grown LuAG:Ce SCF onto a YAG:Ce substrate.

The determination of film thickness was accomplished through the precise weighing of the substrate both before and after the growth cycle of the SCFs. The thickness (h_f) of the SCFs was calculated using the formula:

$$h_f = \frac{m - m_s}{2S\rho} \quad (1)$$

In this equation, m represents the mass of the substrate with the grown SCF in grams (g), m_s is the mass of the substrate in grams, S is the area of the substrate in cm², and ρ is the density of the film in g cm⁻³. The values of densities are $\rho = 4.55 \text{ g cm}^{-3}$ for YAG and $\rho = 6.67 \text{ g cm}^{-3}$ for LuAG.

3. Experimental techniques

XRD measurements

XRD measurements were conducted using a DRON 4 diffractometer with a CuK α X-ray source, covering the 2θ range from 91° to 95° with a step of 0.02°. This was undertaken to determine the structural quality and misfit values between the LuAG:Ce SCF and the YAG:Ce substrate. The diffraction profile of the (888) plane of a LuAG:Ce SCF grown on a YAG:Ce crystal substrate is illustrated in Fig. 2.

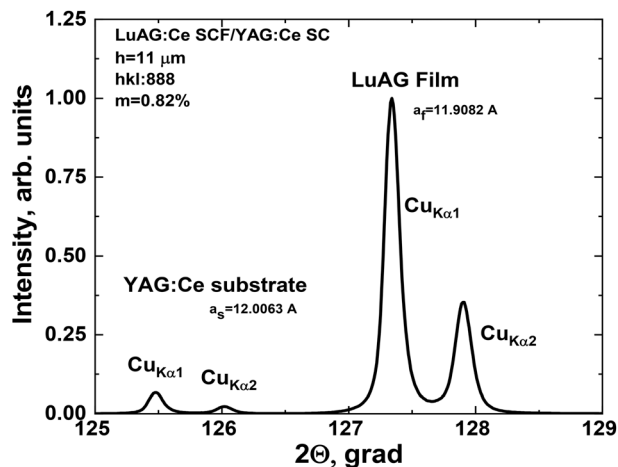


Fig. 2 XRD pattern of the (888) plane of the 11 μm LuAG:Ce film grown onto the [111] oriented YAG:Ce substrate.

The diffraction pattern shows two types of peaks separated from each other, corresponding to reflections from the film and substrate. The peak from the LuAG:Ce film is slightly shifted towards larger angle values due to the decreased lattice constant compared with the YAG:Ce substrate. XRD analysis also verified the exclusive presence of the LuAG phase in the film, with no discernible peaks attributed to other crystalline phases within the precision of the XRD setup. Additionally, the high structural quality of the LuAG:Ce SCF is confirmed by comparing the XRD peak width (Δ) of the epitaxial films with that of the YAG:Ce crystal substrate. Notably, a closely matched value of the peak width ($\Delta = 0.14^\circ$) is observed for the LuAG:Ce SCF, closely aligning with the YAG:Ce crystal value of 0.15° (see Fig. 2). The measured lattice constant of the YAG:Ce crystal substrate was determined as $a_{\text{sub}} = 12.0063 \text{ \AA}$, while the lattice constant of the LuAG:Ce SCF was $a_f = 11.9082 \text{ \AA}$. Consequently, the lattice mismatch between the substrate and the film was estimated as $m = (a_f - a_{\text{sub}})/a_{\text{sub}} \times 100 = -0.82\%$.

Micro-CT measurements

The LPE grown LuAG:Ce SCF onto a YAG:Ce substrate has been meticulously examined using X-ray tomography, providing a detailed insight into the epitaxial structure (see Fig. 3). The tomography structure analysis was performed using a high-resolution Micro-CT Bruker Skyscan 1272 with phase-contrast object shape detection up to $0.4 \mu\text{m}$.

The obtained images reveal a distinct contrast between the left and right pictures. The right image presents a direct visualization of the epitaxial structure, showcasing its inherent features. On the left, a reconstructed image from the tomography process is displayed, where a density filter has been applied to enhance the clarity of the LuAG film and YAG:Ce substrate. The density of the LuAG film is determined to be 6.67 g cm^{-3} , while the YAG:Ce substrate exhibits a density of 4.5 g cm^{-3} . Notably, the substrate density has been muted in the reconstruction, allowing a

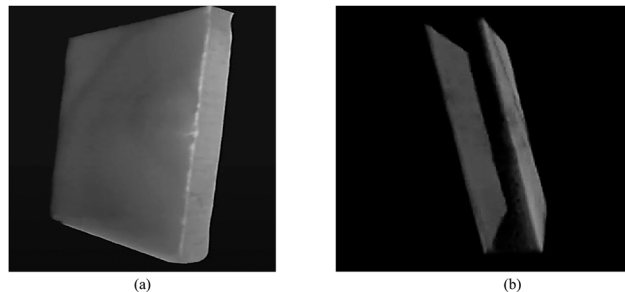


Fig. 3 Micro-CT scan reconstruction of the YAG:Ce substrate (a) and LuAG:Ce single-crystalline film (b) grown on a YAG:Ce substrate.

focused observation of the LuAG film on both sides of the substrate. The epitaxial structure, as depicted in the images, appears to be regular, displaying a commendable uniformity with only minor deviations in thickness. This slight variation can be attributed to the relatively small size of the grown sample. Typically, epitaxial structures for commercial applications are grown on larger substrates, commonly with a diameter of a few inches.

Acoustic microscopy

Acoustic microscopy uses an ultrasonic pulse from the transducer to probe the sample and monitor the reflected echoes from a series of time delays of the pulses induced after interacting with the internal structure. In this research, the $V(z)$ curve method in conjunction with scanning acoustic microscopy was used to evaluate the elastic properties of epitaxial structures. Fig. 4 presents a schematic diagram illustrating the propagation of different types of surface waves (the Rayleigh waves being the most common) between the acoustic lens and the specimen *via* a coupling medium (water).

Rayleigh waves arise at the interface between a solid and non-solid medium, originating from incident waves impinging at the Rayleigh angle θ_R . The generation of a surface acoustic wave at a liquid–solid interface is achievable when the half aperture angle of the acoustic lens exceeds the second critical angle associated with that particular surface. Interference between the specularly reflected acoustic waves (path #1 in Fig. 4) and the surface acoustic waves (path #2) at the acoustic sensor (microscope transducer) leads to the generation of alternating maxima and minima in the acoustic output signal. The occurrence and spacing of these interference patterns depend on the distance between the acoustic lens and the specimen and is commonly referred to as the $V(z)$ curve. The velocity of the surface acoustic wave (SAW) can be determined by measuring the spacing Δz between the consecutive minima in the interference pattern. This arises from considerations of the difference in the path and phase change during the interference of two waves. As the specimen (depicted in Fig. 4) is displaced from $z = 0$ towards the acoustic lens by distance z , paths #1 and #2 undergo distinct phase changes. When the specimen is

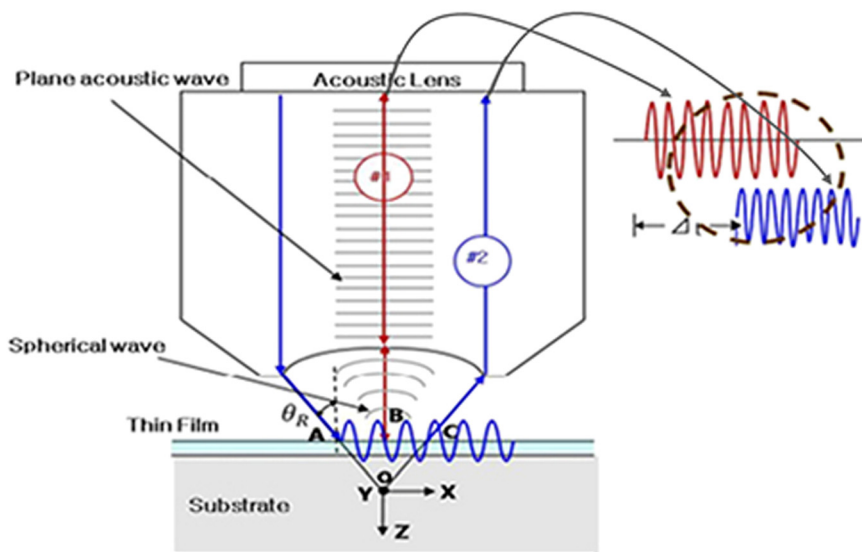


Fig. 4 A schematic diagram that demonstrates the fundamental concept of the $V(z)$ curve.²⁷

positioned at distance z from the focal plane of the lens, the phase changes $\delta_{\#1}$ and $\delta_{\#2}$ can be expressed as follows:²¹

$$\delta_{\#1} = -2\overline{B0} \cdot k_w = -2zk_w, \quad \delta_{\#2} = -2\overline{A0C} \cdot k_w + \overline{AC} \cdot k_r \quad (2.1)$$

The relative phase change between the two paths can be described as follows:

$$\Delta z = \delta_{\#2}(z) - \delta_{\#1}(z) = 2z \left[k_w \left(1 - \frac{1}{\cos \theta_R} \right) + k_r \tan \theta_R \right] \quad (2.2)$$

where k_w is the wavenumber in the water, while k_r is the wavenumber of the surface wave.

Based on eqn (2.2) and applying Snell's law, the following expression can be obtained:

$$\Delta z = \frac{v_w}{2f(1 - \cos \theta_R)} \quad (2.3)$$

Here, v_w represents the acoustic velocity in water, f denotes the working frequency, and the Rayleigh angle is $\sin \theta_R = \frac{v_w}{v_R}$.

In the paper, the $V(z)$ curves were recorded with a custom-made acoustic microscope operated with frequencies at 35,

100, and 200 MHz.³¹ The coupling medium employed in this study to establish the interface between the lens and the specimen was distilled water. All measurements were performed at a constant room temperature throughout the experiment.

In Fig. 5, the images acquired through acoustic microscopy revealing the surface quality are shown. The substrate surface appears smooth and uniform with faint traces of polishing. However, the film, following the growth process, was not subjected to polishing, revealing a non-ideal post-growth surface.

4. Modeling of elastic wave propagation in layered structures

The main aim of the application of acoustic microscopy to study the composite material is the determination of the $V(z)$ curve.^{24,25} Analysis of the $V(z)$ curve in connection with an appropriate model of wave propagation in the material can be used for the effective extraction of the material properties. The elastic waves propagating in layered structures are guided and the phase velocities vary with the frequencies. To obtain the dispersion relation, the equations of the motion of plane waves in a liquid and a solid are used to describe the wave propagation in the layered structures. Two simplified models of ultrasonic wave propagation are proposed in this study, corresponding to the measurement conditions of the substrate (designated as model M1) and the substrate with a single crystalline film grown on it (referred to as model M2). The schemes of these models are depicted in Fig. 6.

For the modeling of wave propagation in the YAG substrate with the thickness of $L = 500 \mu\text{m}$, the simplified model of two adjacent half spaces is considered. The upper half-space is occupied by fluid (water) or air, while the lower is by the solid substrate. Considering the

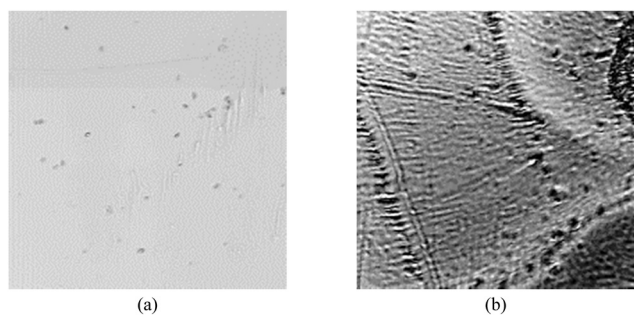


Fig. 5 Acoustic images of the YAG:Ce substrate (a) and LuAG:Ce/YAG:Ce (b) surface.

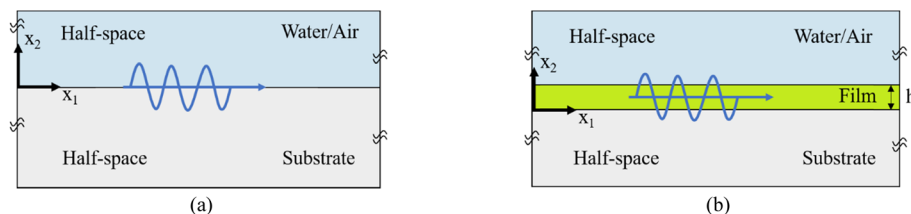


Fig. 6 (a) Fluid/substrate (model M1) and (b) fluid/film/substrate (model M2).

substrate layer as a solid half-space is justified by the fact that the thickness of the substrate (L) is much greater than the wavelengths ($\lambda = 20\text{--}80\ \mu\text{m}$) calculated for the range of frequencies (35–200 MHz) used in acoustic microscopy experiments. Similar reasoning is applied for modeling wave propagation for the YAG:Ce substrate and LuAG:Ce SCF with the thickness of $h \approx 30\ \mu\text{m}$ grown onto it. In this case, two half-spaces of the YAG:Ce substrate and coupling fluid are separated by a thin layer (film). For low frequencies (~ 35 MHz), the wavelengths ($\lambda \sim 80\ \mu\text{m}$) are greater than the film thickness. For the higher frequencies (100 and 200 MHz), the wavelengths ($\lambda = 20\text{--}40\ \mu\text{m}$) became closer to the film thickness and justified the choice of the model.

The guided waves propagate along the x_1 -axis within the x_1 - x_2 plane. The system of displacement components will be expressed in terms of the scalar and vector potential functions.^{23,32}

$$\begin{cases} u_1 = \varphi_{1,1} + \psi_{1,2}, & u_2 = \varphi_{1,2} - \psi_{1,1} \\ u_1^s = \varphi_{2,1} + \psi_{2,2}, & u_1^s = \varphi_{2,2} - \psi_{2,1} \\ u_1^f = \varphi_{3,1}, & u_2^f = \varphi_{3,2} \end{cases} \quad (3.1)$$

where \mathbf{u} , \mathbf{u}^s , and \mathbf{u}^f are the displacement vectors in the film, substrate and fluid layer, respectively (the subscript denotes the component in the x_1 or x_2 direction); φ_i ($i = 1, 2, 3$) is the scalar potential function for the film, substrate and fluid, the vector potential is written similarly ψ_j ($j = 1, 2$), and the partial derivative concerning the coordinate is written as the second subscript.

When considering the guided wave propagating along the x_1 -axis, the corresponding potentials are:

$$\begin{aligned} \varphi_i &= \varphi_{0i}(x_2)\exp[i(kx_1 - \omega t)] \\ \psi_j &= \psi_{0j}(x_2)\exp[i(kx_1 - \omega t)] \end{aligned} \quad (3.2)$$

Substituting this expression to the motion equations for a solid and liquid, we obtain a system of wave equations of the longitudinal and shear waves propagating in the medium:^{23,32}

$$\begin{cases} \frac{\partial^2 \varphi_i}{\partial x_1^2} + \frac{\partial^2 \varphi_i}{\partial x_2^2} = \frac{1}{c_{1i}^2} \frac{\partial^2 \varphi_i}{\partial t^2} \\ \frac{\partial^2 \psi_j}{\partial x_1^2} + \frac{\partial^2 \psi_j}{\partial x_2^2} = \frac{1}{c_{2j}^2} \frac{\partial^2 \psi_j}{\partial t^2} \end{cases} \quad (3.3)$$

where: $c_{1i} = \sqrt{(\lambda_i + 2\mu_i)/\rho_i}$, $c_{13} = \sqrt{\lambda_3/\rho_i}$ and $c_{2j} = \sqrt{\mu_j/\rho_i}$.

The potential components for the solid and fluid can be written as:^{23,32}

$$\begin{cases} \varphi_1 = (a_1 e^{-i\alpha_1 x_2} + b_1 e^{i\alpha_1 x_2}) e^{ikx_1}, & \psi_1 = (c_1 e^{-i\beta_1 x_2} + d_1 e^{i\beta_1 x_2}) e^{ikx_1} \\ \varphi_2 = (a_2 e^{-i\alpha_2 x_2} + b_2 e^{i\alpha_2 x_2}) e^{ikx_1}, & \psi_2 = (c_2 e^{-i\beta_2 x_2} + d_2 e^{i\beta_2 x_2}) e^{ikx_1} \\ \varphi_3 = (a_1 e^{-i\alpha_1 x_2} + b_1 e^{i\alpha_1 x_2}) e^{ikx_1} \end{cases} \quad (3.4)$$

where:

$$\begin{aligned} \alpha_1 &= \sqrt{k_{11}^2 - k^2}, & \alpha_2 &= \sqrt{k_{12}^2 - k^2}, & \alpha_3 &= \sqrt{k_{12}^2 - k^2}, \\ \beta_1 &= \sqrt{k_{11}^2 - k^2}, & \beta_2 &= \sqrt{k_{12}^2 - k^2}, \\ k_{11} &= \omega/c_{11}, & k_{12} &= \omega/c_{12}, & k_{13} &= \omega/c_{13}, & k_{t1} &= \omega/c_{t1}, & k_{t2} &= \omega/c_{t2}. \end{aligned}$$

To ensure that there are no displacements in both the substrate layer and the fluid as x_2 approaches infinity, the values of b_2 and d_2 should be 0, and similarly, $a_3 = 0$.

The equations describing the stresses in each layer look like the following:²³

$$\begin{cases} \sigma_{ij} = \mu_1 (u_{i,j} + u_{j,i}) + \lambda_1 u_{k,k} \delta_{ij} \\ \sigma_{ij}^s = \mu_2 (u_{i,j}^s + u_{j,i}^s) + \lambda_2 u_{k,k}^s \delta_{ij} \\ p = -\lambda_3 u_{k,k}^f \end{cases} \quad (3.5)$$

In the context of stress and pressure at a fluid–solid interface, the Cauchy stress in the thin elastic layer and substrate layer is denoted σ_{ij} and σ_{ij}^s , respectively. The pressure exerted by the fluid is represented by the symbol p .^{23,32}

To find analytical solutions for both models, the relationships concerning the displacements eqn (3.1) and stress components eqn (3.5) for a specific medium need to satisfy specific interfacial boundary conditions (ICs). For both models, we will consider that the upper half-space can be occupied by liquid fluid (water or air), and thus two sets of ICs are proposed:

- Interfacial boundary conditions ($x_2 = 0$) for model M1:

$$\begin{array}{cc} \text{Water} & \text{Air} \\ \left\{ \begin{array}{l} u_2^s = u_2^f \\ \sigma_{22}^s = 0 \\ \sigma_{12}^s = 0 \end{array} \right. & \mathbf{x}_2 = \mathbf{0} & \left\{ \begin{array}{l} \sigma_{22}^s = 0 \\ \sigma_{12}^s = 0 \end{array} \right. \end{array} \quad (3.6)$$

- Interfacial boundary conditions ($x_2 = 0$ and $x_2 = h$) for model M2:

$$\begin{array}{l}
 \text{Water} \\
 \left\{ \begin{array}{l} u_1 = u_1^s \\ u_2 = u_2^s \\ \sigma_{22} = \sigma_{22}^s \\ \sigma_{12} = \sigma_{12}^s \end{array} \right. \\
 \\
 \left\{ \begin{array}{l} u_2 = u_2^f \\ \sigma_{22} = -p \\ \sigma_{12} = 0 \end{array} \right. \\
 \\
 \text{Air} \\
 \left\{ \begin{array}{l} u_1 = u_1^s \\ u_2 = u_2^s \\ \sigma_{22} = \sigma_{22}^s \\ \sigma_{12} = \sigma_{12}^s \end{array} \right. \\
 \\
 \left\{ \begin{array}{l} u_2 = u_2^f \\ \sigma_{12} = 0 \end{array} \right.
 \end{array}
 \quad
 \begin{array}{l}
 x_2 = 0 \\
 \\
 \\
 \\
 x_2 = h
 \end{array}
 \quad
 (3.7)$$

Substitution of appropriate expressions for the displacements eqn (3.1) and stresses eqn (3.5) into interfacial conditions eqn (3.6) or eqn (3.7) leads to a set of linear algebraic equations, which can be generally written in a matrix form as:

$$\mathbf{M}[a_1, b_1, c_1, d_1, a_2, c_2, b_3]^T = 0. \quad (3.8)$$

The matrix \mathbf{M} for both models (M1 and M2) is a function of the Lamé constants (λ , μ), densities of the components (ρ_i), the layer thickness (h) and frequency (f). The exact form of the matrices is presented in the Appendix.

The requirement for the existence of nontrivial solutions of eqn (3.8) is that:

$$\det(\mathbf{M}) = 0, \quad (3.9)$$

determines the dispersion relationships of the guided waves, which can be used for the evaluation of phase velocity as a function of frequency.

5. Acoustic microscopy investigation of the YAG:Ce substrate and LuAG:Ce film/YAG:Ce crystal epitaxial structure

For both samples (the YAG:Ce crystal substrate and LuAG:Ce film/YAG:Ce crystal epitaxial structure), a $V(z)$ curve was obtained by using an acoustic microscope. The velocity of the surface acoustic wave (SAW) can be determined by measuring the spacing Δz between consecutive minima in the interference pattern ($V(z)$ curve – see Fig. 6). This arises from

the considerations of the difference in the path and phase change during the interference of two waves. The Δz value was measured for each specimen at different wave frequencies ($f = 35$; $f = 100$; $f = 200$ MHz), and the SAW velocity was calculated using the following formula:²⁷

$$V_{\text{SAW}} = \frac{v_w}{\sqrt{1 - \left(1 - \frac{v_w}{2f\Delta z}\right)^2}} \quad (4.1)$$

where v_w represents the acoustic velocity in water. To minimize measurement errors, the $V(z)$ curve was measured 5 times for each sample at different positions of their surfaces.

First, acoustic microscopy measurements were performed for the YAG:Ce crystal substrate. Fig. 7 demonstrates the exemplary $V(z)$ curve for the YAG:Ce substrate sample with a thickness of 500 μm obtained using a 200 MHz transducer.

The velocity of the surface acoustic wave was determined by measuring the spacing Δz between successive minima and maxima in the $V(z)$ curve pattern. The calculated phase velocities measured at different excitation frequencies for the YAG:Ce substrate are presented in Table 1.

It can be seen from the table that measured values of the phase velocity are very close and weakly depend on the frequency of the excitation wave. Thus, we conclude that the dispersion in the experimental frequency range (35–200 MHz) is small. The wavelengths calculated as a ratio of wave velocity and transducer frequency ($\lambda = \text{velocity/frequency}$) range from 130 μm (for a 35 MHz transducer) to 23 μm (for a 200 MHz transducer). The obtained results for the YAG:Ce crystal substrate are expected because the above-mentioned wavelengths are at least 5 times smaller than the substrate thickness (500 μm). Thus, it seems justified to conclude that in this case, a nondispersive surface Rayleigh type of wave propagates in the YAG:Ce substrate material. In the second stage, the $V(z)$ acoustic curves for the epitaxial structures at different frequencies were measured. In Fig. 6b, the exemplary curve measured using a 100 MHz transducer is shown for the epitaxial structure containing the YAG:Ce crystal substrate with 500 μm thickness covered by the LuAG:Ce SCF with a thickness of ~ 30 μm from both sides. The calculated values of the phase velocities obtained at three

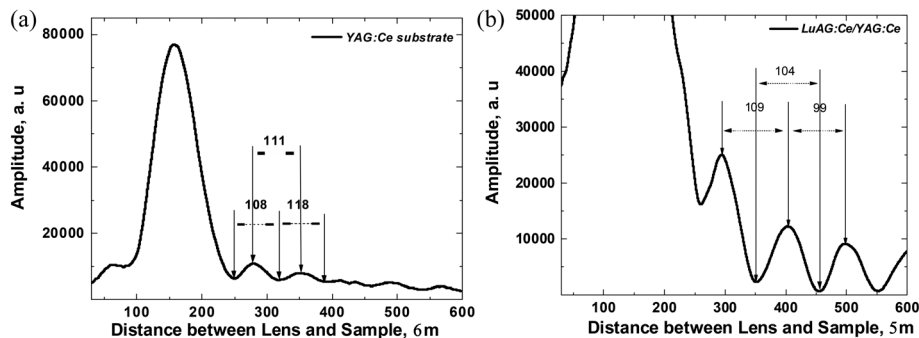


Fig. 7 (a) Exemplary $V(z)$ curve for the YAG:Ce crystal substrate measured using a 200 MHz transducer and (b) for the LuAG:Ce SCF/YAG:Ce crystal substrate epitaxial structure measured using a 100 MHz transducer.

Table 1 Measured phase velocities for three frequencies in the YAG:Ce crystal substrate and LuAG:Ce SCF/YAG:Ce crystal epitaxial structure

Frequency, MHz	YAG:Ce SC	LuAG:Ce SCF/YAG:Ce crystal
	Phase velocity, m s ⁻¹	Phase velocity, m s ⁻¹
35	4633 ± 57	4177 ± 95
100	4648 ± 33	3986 ± 150
200	4596 ± 45	5052 ± 135

Table 2 Input (initial) parameters for the numerical calculations of the models

Parameter	Symbol	Value
Density of bulk substrate YAG:Ce	ρ^s	6000 [g cm ⁻³]
Density of bulk film LuAG:Ce	ρ^l	4500 [g cm ⁻³]
Density of the fluid	ρ_f	1000 [g cm ⁻³]
Density of the air	ρ_a	1 [g cm ⁻³]
Speed of sound in the fluid	V_f	1500 [m s ⁻¹]
Velocity of a longitudinal and shear wave in the YAG:Ce crystal substrate	c_{L}^s, c_{SH}^s	8500, 5070 [m s ⁻¹]
The velocity of a longitudinal and shear wave in the LuAG:Ce film	c_{L}^l, c_{SH}^l	7000, 4500 [m s ⁻¹]

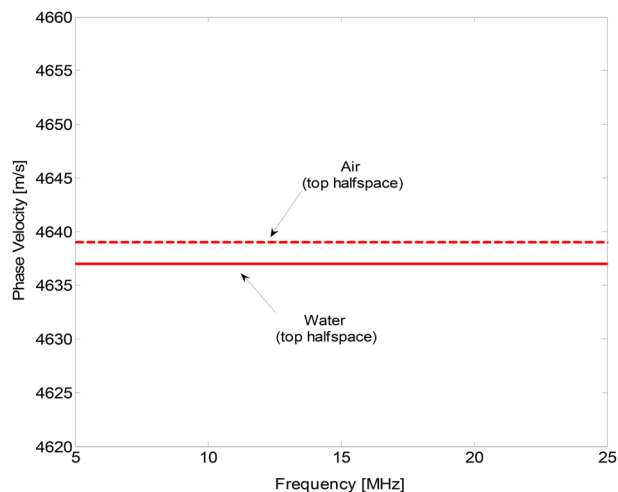
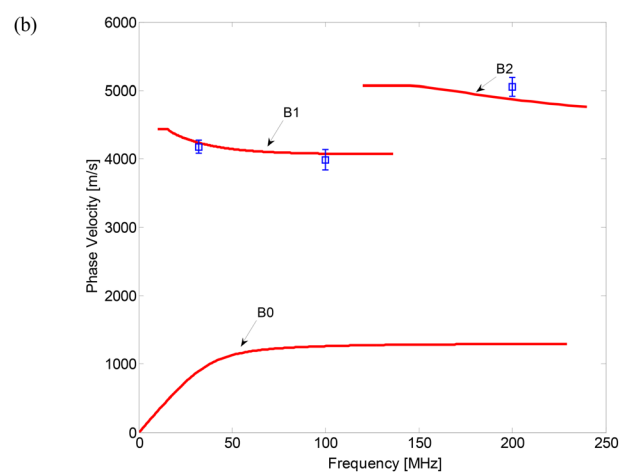
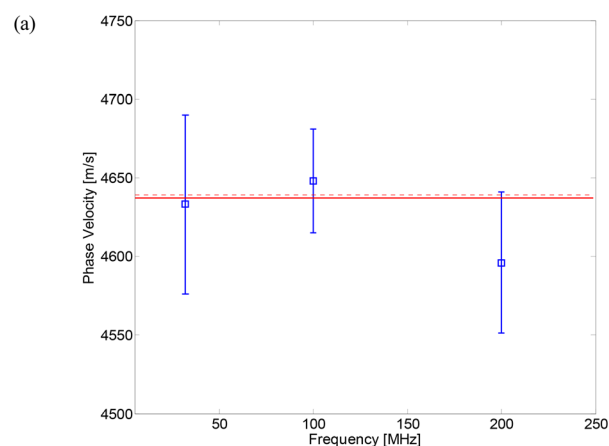
frequencies are summarized in Table 1. The SAWs in the epitaxial structure exhibit a dispersive nature, meaning that their phase velocity depends on their frequency. This dispersion is a consequence of the complex interaction of the surface wave with the layered structure of the material.

6. Comparison of model predictions with experimental results

To obtain a dispersion curve experimentally, a significant number of measurements need to be conducted using ultrasonic transducers with a precise frequency increment. The other solution is to use the wideband transducers and

ultrasonic spectroscopy method. The above-mentioned experimental methods are difficult to apply for samples of small dimensions. Thus, the present study employs an alternative approach that involves the validation of experimental data by comparing them to predictions derived from a theoretical model. Solving numerical models of physical processes is crucial as it provides a deeper understanding of complex phenomena and enables the exploration of inaccessible conditions. In the paper, the MATLAB programming software was used to solve numerically the dispersion equations.

Initially, the microscopic material parameters used in the model were taken from the literature.^{26,27} Table 2 presents a

**Fig. 8** Phase velocity dispersion curve for the M1 model (two-adjacent half-spaces). The upper half-space is occupied by water or air while the bottom half-space is by the YAG:Ce SC substrate.**Fig. 9** Comparison of calculated (red continuous and dotted line) and measured (blue squares) phase velocities for YAG:Ce substrate (a) and for YAG:Ce/LuAG:Ce epitaxial structure (b).

list of initial parameters that were utilized in the numerical calculations related to the M1 and M2 models.

Fig. 8 demonstrates the numerically calculated dispersion curves for the M1 model. To simulate experimental conditions, two cases were examined *i.e.* the case when the upper half-space is occupied by water or air while the bottom half-space was the YAG:Ce crystal substrate.

In ultrasonic microscopy experiments, the focused probe is immersed in water (coupling medium) to ensure the transmission of the wave to the sample. The wave propagates mainly in the solid sample, but some of its energy leaks to the coupling medium which, in general, may lead to the dispersion. The results presented in Fig. 8 show that the theoretical predictions of the dispersion curves differ very little when the water is replaced by air (within 2–3 m s⁻¹). Thus, we conclude that the presence of water or air in the top half-space practically does not influence the wave velocity in the substrate (solid) and in further analysis, a simplified model (with air in the upper half-space) will be used.

In Fig. 9a, the experimental results (from ultrasonic microscopy) with error bars for the YAG:Ce crystal substrate are compared with the dispersion curves numerically calculated for the simplified M1 model. The experimental values overlap to a large extent with the simulated results in the low-frequency region. For a frequency of 200 MHz, there is a deviation of the experimental data to the region

of lower phase velocities, which can be associated with experimental errors.

In Fig. 9b, a similar comparison of the measured and theoretically predicted phase velocity dispersions for the epitaxial structure of the LuAG:Ce SCF/YAG:Ce crystal is shown. Within the considered frequency range, the theory predicted the existence of three different modes (B0, B1, B2). The B0 (fundamental) mode exists in the whole frequency range, while the higher order modes (B1, B2) are at the higher frequencies only. Based on the results shown in Fig. 9a and b, one can conclude that in the experiments for the epitaxial structure of the LuAG:Ce SCF/YAG:Ce crystal, only B1 and B2 wave modes are observed. The absence of experimental results lying in the region of the B0 mode is most likely associated with the sensitivity of the measuring equipment.

7. Extraction of material properties based on the optimization procedure

The model's accuracy and reliability need to be assessed by comparing its predictions with experimental data from well-designed experiments. This validation process helps establish confidence in the model's ability to accurately represent the physical process under investigation. The optimization procedure involves comparing the calculated or predicted wave modes with the experimental results.

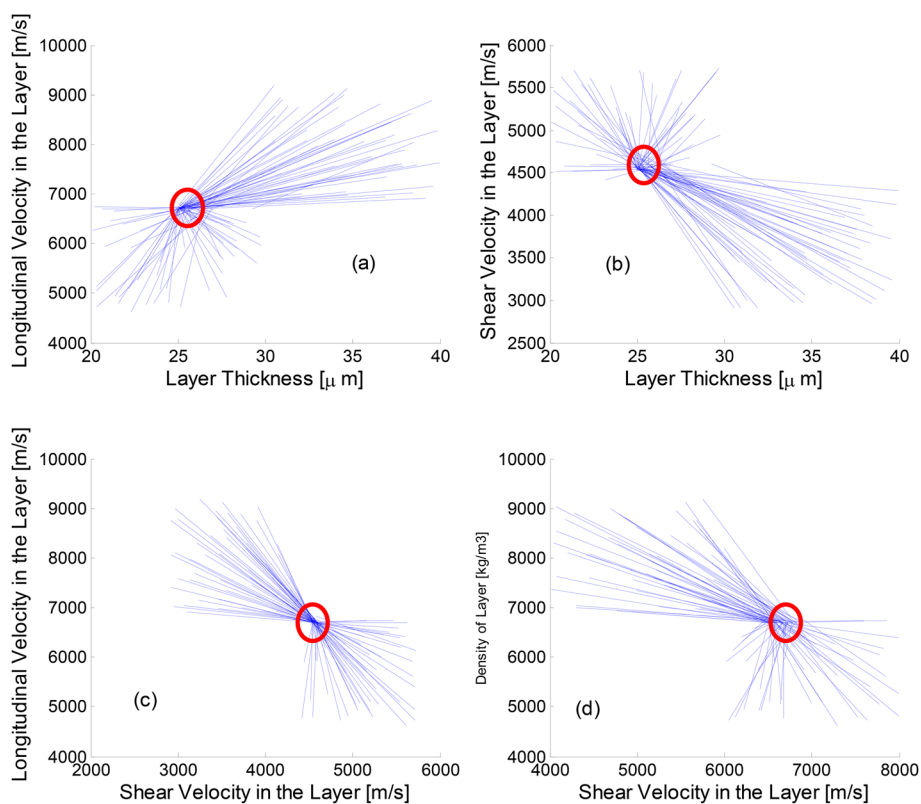


Fig. 10 The estimation of convergence of the optimization procedure: (a) – longitudinal velocity depends on layer thickness, (b) – shear velocity depends on layer thickness, (c) – longitudinal velocity depends on shear velocity, and (d) – density of the layer depends on shear velocity.

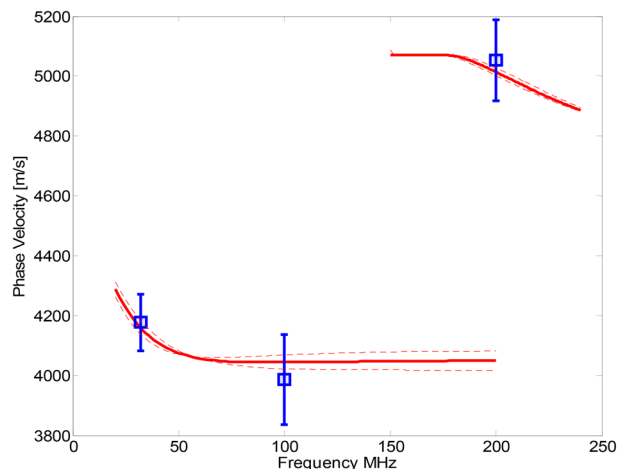


Fig. 11 Dispersion curves for the LuAG:Ce SCF/YAG:Ce crystal epitaxial structure. The dotted line shows the dependence for the minimum and maximum values of the parameters, and the solid line shows the optimal curve. The minimum optimal and maximum values are summarized in Table 3.

This process aims to find the best set of parameters or conditions that can reproduce the observed modes most accurately. During the optimization, various parameters related to the material properties or experimental setup may be adjusted or fine-tuned. These parameters can include dimensions, compositions, boundary conditions, or any other relevant variables that affect the wave modes. The optimization procedure typically involves iterative steps, where the calculated values are compared with the experimental data. Based on the level of agreement or discrepancy between the two, the parameters are adjusted, and the calculation is repeated. In the context of modeling, optimization is often used to minimize a cost function. The cost function represents the measure of error or discrepancy between the predicted and actual values.

In the context of this work, a standard genetic algorithm toolbox embedded in the MATLAB libraries was chosen.³³ The cost function (CF) is defined as follows:

$$CF = \sum_{i=1}^N [v_i(f) - c(\mathbf{b}, f_i)]^2 \quad (5.1)$$

where:

v_i – vector experimental phase velocities,

f – frequency,

c – model predictions (phase velocity) for a given frequency (f) and,

\mathbf{b} – vector of identified parameters [c_L^1 , c_{SH}^1 , ρ^1 , h].

Since the ultimate goal is to determine the mechanical parameters of the LuAG:Ce SCF, first the optimization of the parameters for the YAG:Ce substrate was performed, and then these values were used in the optimization procedure for the LuAG:Ce SCF/YAG:Ce SC epitaxial structure.

The estimation of convergence of the optimization procedure for four identified parameters of the film is shown in Fig. 10. It is a visualization of the initial and final (after optimization) pairs of identified parameters. The red circle shows the area of convergence of the parameters.

Based on the minimum, optimal, and maximum values of the identified parameters (obtained from the optimization procedure), three dispersion curves for the LuAG:Ce SCF/YAG:Ce SC epitaxial structure were plotted together with the experimental values observed for the B1 and B2 modes (see Fig. 11).

Table 3 summarizes the results obtained from the optimization procedure. The mechanical properties (Young modulus and Poisson ratio) are calculated based on the optimal values of the velocities of the longitudinal and shear waves and the density of the layer using the well-known formulas, which can be found elsewhere.¹⁷

At present, the literature remains devoid of information concerning the mechanical properties of LuAG:Ce in the SCF form. Table 4 shows the values for LuAG in the single crystal and ceramic forms,^{34–36} which could be found in the literature in comparison to optimal values obtained for LuAG:Ce SCFs. As can be seen from Table 4, the mechanical properties of the crystals are approximately the same, while the ceramics have slightly lower values, which are explained by the presence of a significant content of air pores in the ceramics. The density value for the LuAG film ($6799 \pm 149 \text{ kg m}^{-3}$) slightly exceeds the literature values for single crystals. Such difference can be explained by the large concentration of Lu_{Al} antisite defects in the LuAG crystals, grown from the high-temperature melt and non-stoichiometric composition $\text{Lu}_3\text{Lu}_x\text{Al}_{5-x}\text{O}_{12}$ of these crystals, where $x = 0.024$.³⁷

The values of Young's modulus and Poisson's coefficient are in line with literature values, but it's important to note that direct comparisons cannot be made with materials in different crystalline forms. It's worth emphasizing once more that there is currently no existing literature that specifically investigates the mechanical properties of garnet SCFs. It's crucial to recognize that the low-temperature melt growth technique results in a minimal concentration of

Table 3 Mechanical properties of the LuAG:Ce film obtained from the optimization procedure. E – Young modulus; ν – Poisson ratio

Parameter	Minimum value	Optimal value	Maximum value
E , [GPa]	278	290	302
ν	0.22	0.23	0.24
Film thickness [μm]	21	22	23
Film density [kg m^{-3}]	6650	6799	6948

Table 4 Mechanical properties of LuAG bulk crystals and ceramics^{32,38–41}

Source	C_{11}	C_{44}	E [GPa]	ν	ρ [g cm ⁻³]
M. J. Weber <i>et al.</i> ³⁴ values for bulk crystals	339	113	282.7	0.251	6.71
P. D. Dragic <i>et al.</i> ³⁵ values for bulk crystals	342	115	286.7	0.246	6.71
Fu <i>et al.</i> ³⁶ values for LuAG:Yb ceramics	—	—	275	—	6.65
Our results	320	122	290	0.23	6.8

defects in these materials, distinguishing them from counterparts in different crystalline forms. Consequently, we have successfully determined the elastic properties of LuAG:Ce SCFs for the first time.

Conclusions

As part of theoretical and numerical research, a microscopic model for a layered epitaxial structure was developed to explain the propagation of ultrasonic waves with wavelengths comparable to the thickness of the film. The dispersion equations for two models were obtained, which are defined by the mechanical and acoustical properties of materials. The measurements using acoustic microscopy were conducted to determine the phase velocity of acoustic surface waves on the YAG:Ce crystal substrate and the LuAG:Ce SCF/YAG:Ce SC epitaxial structure. The resultant phase velocities (~ 4600 m s⁻¹) at distinct excitation frequencies for the YAG:Ce crystal substrate are very close and weakly depend on the frequency of the excitation wave. However, the surface acoustic waves in the epitaxial structure exhibit a dispersive nature, meaning that their phase velocity depends on their frequency. This dispersion is a consequence of the complex interaction of the surface wave with the layered structure of the material.

It is concluded that the presence of water or air has a negligible effect on wave velocity in the substrate, leading to the use of a simplified model with air in the upper half-space for further analysis. A specific optimization sequence is described, starting with the optimization of parameters for the YAG substrate. The values obtained in this initial step are then utilized in the optimization procedure for the LuAG:Ce SCF/YAG:Ce crystal epitaxial structure.

Experimental results, obtained through ultrasonic microscopy, were compared with the dispersion curves numerically calculated for the considered model. This comparison reveals a high degree of agreement in the low-frequency region, with slight deviations at higher frequencies, possibly attributed to experimental errors. The optimization procedure for extracting material properties illustrates its practical implementation in analyzing the LuAG:Ce SCF/YAG:Ce crystal epitaxial structure and offers valuable insights into the mechanical characteristics of this material. The obtained values of Young's modulus (290 ± 12 GPa) and Poisson's coefficient (0.22 ± 0.01) are in line with the results found in the literature. This highlights the unique and pioneering aspect of this research, specifically in

uncovering the elastic properties of LuAG:Ce SCFs, the well-known scintillation materials, an area that had remained unexplored in prior literature.

Data availability

The data supporting the findings of this study, titled "Acoustic microscopy study on elasto-mechanical properties of Lu₃Al₅O₁₂:Ce single crystalline films" (Manuscript ID: CE-ART-01-2025-000068), can be found in the repository. The data is accessible at the following link: <https://repop.icm.edu.pl/dataset.xhtml?persistentId=doi:10.18150/BNMREE>.

Author contributions

Anton Markovskiy and Michał Rosiak analyzed the experimental materials and drafted the manuscript. Vitalii Gorbenko performed the growth of LuAG:Ce SCFs using the LPE method. Yuriy Zorenko contributed in the methodology and resources of the experiment and corrected the draft of the paper. The XRD measurements were performed by Alexander Fedorov. The micro-CT measurements were performed and analyzed by Zbigniew Szczepański and Mieczysław Ciezko. The experimental data from acoustic microscopy were obtained by Jerzy Litniewski. The interpretation of the results and the optimization procedure were carried out by Mariusz Kaczmarek and Michał Pakuła.

Conflicts of interest

The authors declare no conflict of interest.

Appendix

For model M1 and the liquid in the upper half space, the matrix (3×3) can be written as:

$$M_1^{\text{water}} = \begin{bmatrix} -\alpha_2 & -k & \alpha_3 \omega \\ \mu_2 k^2 & 2\mu_2 k \beta_2 & 0 \\ 2\mu_2 k \alpha_2 & \mu_2 k^2 & 0 \end{bmatrix} \quad (\text{A.1})$$

where $k^2 = (k^2 - \beta_2^2)$.

When the water is replaced by air, the simplified version (2×2) of the relationship eqn (A.1) can be derived:

$$M_1^{\text{air}} = \begin{bmatrix} \mu_2 k^2 & 2\mu_2 k \beta_2 \\ 2\mu_2 k \alpha_2 & \mu_2 k^2 \end{bmatrix} \quad (\text{A.2})$$

In turn, for model M2 and the liquid in the upper half space, the matrix (7×7) can be written as:

$$M_2^{liquid} = \begin{bmatrix} k & k & -\beta_1 & \beta_1 & -k & \beta_2 & 0 \\ -\alpha_1 & \alpha_1 & -k & -k & \alpha_2 & k & 0 \\ \mu_1 k_1^2 & \mu_1 k_1^2 & -2\mu_1 k \beta_1 & 2\mu_1 k \beta_1 & -\mu_2 k_2^2 & 2\mu_2 k \beta_2 & 0 \\ 2\mu_1 k \alpha_1 & -2\mu_1 k \alpha_1 & \mu_1 k_1^2 & \mu_1 k_1^2 & -2\mu_2 k \alpha_2 & -\mu_2 k_2^2 & 0 \\ -\alpha_1 e^{-i\alpha_1 h} & \alpha_1 e^{i\alpha_1 h} & -k e^{-i\beta_1 h} & -k e^{i\beta_1 h} & 0 & 0 & -\alpha_3 \omega e^{i\alpha_3 h} \\ \mu_1 k_1^2 e^{-i\alpha_1 h} & \mu_1 k_1^2 e^{i\alpha_1 h} & -2\mu_1 k \beta_1 e^{-i\beta_1 h} & 2\mu_1 k \beta_1 e^{i\beta_1 h} & 0 & 0 & \lambda_3 (\alpha_3^2 + k^2) e^{i\alpha_3 h} \\ 2k \alpha_1 e^{-i\alpha_1 h} & -2k \alpha_1 e^{i\alpha_1 h} & k_1^2 e^{-i\beta_1 h} & k_1^2 e^{i\beta_1 h} & 0 & 0 & 0 \end{bmatrix} \quad (\text{A.3})$$

where $k_1^2 = k^2 - \beta_1^2$.

When the water half-space is replaced by air half-space, the simplified (6×6) version of the relationship eqn (A.3) can be derived:

$$M_2^{air} = \begin{bmatrix} k & k & -\beta_1 & \beta_1 & -k & \beta_2 \\ -\alpha_1 & \alpha_1 & -k & -k & \alpha_2 & k \\ \mu_1 k_1^2 & \mu_1 k_1^2 & -2\mu_1 k \beta_1 & 2\mu_1 k \beta_1 & -\mu_2 k_2^2 & 2\mu_2 k \beta_2 \\ 2\mu_1 k \alpha_1 & -2\mu_1 k \alpha_1 & \mu_1 k_1^2 & \mu_1 k_1^2 & -2\mu_2 k \alpha_2 & -\mu_2 k_2^2 \\ -\alpha_1 e^{-i\alpha_1 h} & \alpha_1 e^{i\alpha_1 h} & -k e^{-i\beta_1 h} & -k e^{i\beta_1 h} & 0 & 0 \\ 2k \alpha_1 e^{-i\alpha_1 h} & -2k \alpha_1 e^{i\alpha_1 h} & k_1^2 e^{-i\beta_1 h} & k_1^2 e^{i\beta_1 h} & 0 & 0 \end{bmatrix} \quad (\text{A.4})$$

Acknowledgements

The work was performed in the frame of Polish NCN 2022/45/B/ST8/01757 projects and partly in the frame of NCN 2022/31/B/ST8/03390 and Regional Excellence Initiative RID/SP/0048/2024/01 projects.

References

- 1 K. Bartosiewicz, A. Markovskiy, T. Horiai, D. Szymański, S. Kurosawa, A. Yamaji, A. Yoshikawa and Y. Zorenko, A study of Mg²⁺ ions effect on atoms segregation, defects formation, luminescence and scintillation properties in Ce³⁺ doped Gd₃Al₂Ga₃O₁₂ single crystals, *J. Alloys Compd.*, 2022, **905**, 164154, DOI: [10.1016/j.jallcom.2022.164154](https://doi.org/10.1016/j.jallcom.2022.164154).
- 2 A. Markovskiy, W. Gieszczyk, P. Bilski, A. Fedorov, K. Bartosiewicz, K. Paprocki, T. Zorenko and Y. Zorenko, Composition engineering of Tb₃-xGd_xAl₅-yGayO₁₂:Ce single crystals and their luminescent, scintillation and photoconversion properties, *J. Alloys Compd.*, 2020, **849**, 155808, DOI: [10.1016/j.jallcom.2020.155808](https://doi.org/10.1016/j.jallcom.2020.155808).
- 3 K. Bartosiewicz, A. Markovskiy, T. Zorenko, A. Yoshikawa, S. Kurosawa, A. Yamaji and Y. Zorenko, New Efficient Scintillating and Photoconversion Materials Based on the Self-Flux Grown Tb₃Al₅O₁₂:Ce Single Crystal, *Phys. Status Solidi - Rapid Res. Lett.*, 2020, **14**, 2000327, DOI: [10.1002/pssr.202000327](https://doi.org/10.1002/pssr.202000327).
- 4 K. Bartosiewicz, V. Babin, A. Beitlerova, P. Bohacek, K. Jurek and M. Nikl, The temperature dependence studies of rare-earth (Dy³⁺, Sm³⁺, Eu³⁺ and Tb³⁺) activated Gd₃Ga₃Al₂O₁₂ garnet single crystals, *J. Lumin.*, 2017, **189**, 126–139, DOI: [10.1016/j.jlumin.2016.09.053](https://doi.org/10.1016/j.jlumin.2016.09.053).
- 5 K. Bartosiewicz, T. Horiai, A. Yamaji, A. Yoshikawa, S. Kurosawa, M. Yoshino and Y. Zorenko, Effects of La doping on the crystal growth, phase stability and scintillation properties of Lu₃Al₅O₁₂ single crystals, *Mater. Sci. Eng., B*, 2020, **261**, 114677, DOI: [10.1016/j.mseb.2020.114677](https://doi.org/10.1016/j.mseb.2020.114677).
- 6 K. Bartosiewicz, Elemental Fluctuation in Gd₃Al₂Ga₃O₁₂:Ce Crystals Imposed by Li⁺ and Mg²⁺ Co-Doping: The Impact on Defects, Luminescence, and Scintillation Properties, *Metals*, 2023, **13**, 422, DOI: [10.3390/met13020422](https://doi.org/10.3390/met13020422).
- 7 M. Nikl, A. Yoshikawa, K. Kamada, K. Nejezchleb, C. R. Stanek, J. A. Mares and K. Blazek, Development of LuAG-based scintillator crystals – A review, *Prog. Cryst. Growth Charact. Mater.*, 2013, **59**, 47–72, DOI: [10.1016/j.pcrysgrow.2013.02.001](https://doi.org/10.1016/j.pcrysgrow.2013.02.001).
- 8 C. Dujardin, C. Mancini, D. Amans, G. Ledoux, D. Abler, E. Auffray, P. Lecoq, D. Perrodin, A. Petrosyan and K. L. Ovanesyan, LuAG:Ce fibers for high energy calorimetry, *J. Appl. Phys.*, 2010, **108**, 013510, DOI: [10.1063/1.3452358](https://doi.org/10.1063/1.3452358).
- 9 A. G. Petrosyan, K. L. Ovanesyan, R. V. Sargsyan, G. O. Shirinyan, D. Abler, E. Auffray, P. Lecoq, C. Dujardin and C. Pedrini, Bridgman growth and site occupation in LuAG:Ce scintillator crystals, *J. Cryst. Growth*, 2010, **312**, 3136–3142, DOI: [10.1016/j.jcrysgro.2010.07.042](https://doi.org/10.1016/j.jcrysgro.2010.07.042).
- 10 J. Li, S. Sahi, M. Groza, Y. Pan, A. Burger, R. Kenarangui and W. Chen, Optical and Scintillation Properties of Ce³⁺-Doped LuAG and YAG Transparent Ceramics: A Comparative Study, *J. Am. Ceram. Soc.*, 2017, **100**, 150–156, DOI: [10.1111/jace.14461](https://doi.org/10.1111/jace.14461).

- 11 H. Li, X. Liu and L. Huang, Fabrication of Transparent Cerium-Doped Lutetium Aluminum Garnet (LuAG:Ce) Ceramics by a Solid-State Reaction Method, *J. Am. Ceram. Soc.*, 2005, **88**, 3226–3228, DOI: [10.1111/j.1551-2916.2005.00554.x](https://doi.org/10.1111/j.1551-2916.2005.00554.x).
- 12 P. Prusa, J. A. Mares, M. Nikl, M. Kucera, K. Nitsch and M. Hanus, Scintillation properties of LuAG:Ce single crystalline films grown by LPE method, *Opt. Mater.*, 2010, **32**, 1360–1363, DOI: [10.1016/j.optmat.2010.04.010](https://doi.org/10.1016/j.optmat.2010.04.010).
- 13 T. Zorenko, V. Gorbenko, T. Vozniak, S. Heinrich, G. Huber and Y. Zorenko, Comparison of the luminescent properties of LuAG:Ce films grown by pulse laser deposition and liquid phase epitaxy methods using synchrotron radiation excitation, *Opt. Mater.*, 2020, **105**, 109751, DOI: [10.1016/j.optmat.2020.109751](https://doi.org/10.1016/j.optmat.2020.109751).
- 14 P.-A. Douissard, T. Martin, F. Riva, Y. Zorenko, T. Zorenko, K. Paprocki, A. Fedorov, P. Bilski and A. Twardak, Epitaxial Growth of LuAG:Ce and LuAG:Ce,Pr Films and Their Scintillation Properties, *IEEE Trans. Nucl. Sci.*, 2016, **63**, 1726–1732, DOI: [10.1109/TNS.2016.2565731](https://doi.org/10.1109/TNS.2016.2565731).
- 15 Y. Zorenko, V. Gorbenko, A. Voloshinovskii, G. Stryganyuk, V. Mikhailin, V. Kolobanov, D. Spassky, M. Nikl and K. Blazek, Exciton-related luminescence in LuAG:Ce single crystals and single crystalline films, *Phys. Status Solidi A*, 2005, **202**, 1113–1119, DOI: [10.1002/pssa.200420007](https://doi.org/10.1002/pssa.200420007).
- 16 M. Kučera, K. Nitsch, M. Nikl and M. Hanuš, Defects in Ce-doped LuAG and YAG scintillation layers grown by liquid phase epitaxy, *Radiat. Meas.*, 2010, **45**, 449–452, DOI: [10.1016/j.radmeas.2009.12.031](https://doi.org/10.1016/j.radmeas.2009.12.031).
- 17 P. Horodysky, J. Tous, K. Blazek, M. Nikl, Y. Zorenko and M. Kucera, Thin imaging screens based on Ce-doped lutetium–aluminum garnets, *Radiat. Meas.*, 2010, **45**, 628–630, DOI: [10.1016/j.radmeas.2009.12.021](https://doi.org/10.1016/j.radmeas.2009.12.021).
- 18 T. W. Kang, K. W. Park, J. H. Ryu, S. G. Lim, Y. M. Yu and J. S. Kim, Strong thermal stability of Lu₃Al₅O₁₂:Ce³⁺ single crystal phosphor for laser lighting, *J. Lumin.*, 2017, **191**, 35–39, DOI: [10.1016/j.jlumin.2017.01.032](https://doi.org/10.1016/j.jlumin.2017.01.032).
- 19 Liquid Phase Epitaxy of Electronic, Optical and Optoelectronic Materials | Wiley, Wiley.Com (n.d.), <https://www.wiley.com/en-gb/Liquid+Phase+Epitaxy+of+Electronic%2C+Optical+and+Optoelectronic+Materials-p-9780470852903> (accessed April 11, 2024).
- 20 A. Muñoz and P. Rodríguez-Hernández, First-Principle Study of Ca₃Y₂Ge₃O₁₂ Garnet: Dynamical, Elastic Properties and Stability under Pressure, *Crystals*, 2023, **13**, 29, DOI: [10.3390/cryst13010029](https://doi.org/10.3390/cryst13010029).
- 21 V. F. Kitaeva, E. V. Zharikov and I. L. Chisty, The properties of crystals with garnet structure, *Phys. Status Solidi A*, 1985, **92**, 475–488, DOI: [10.1002/pssa.2210920217](https://doi.org/10.1002/pssa.2210920217).
- 22 J. G. Fujimoto, W. Z. Lin, E. P. Ippen, C. A. Puliafito and R. F. Steinert, Time-resolved studies of Nd:YAG laser-induced breakdown. Plasma formation, acoustic wave generation, and cavitation, *Invest. Ophthalmol. Visual Sci.*, 1985, **26**, 1771–1777.
- 23 J. L. Rose, *Ultrasonic Guided Waves in Solid Media*, Cambridge University Press, Cambridge, 2014, DOI: [10.1017/CBO9781107273610](https://doi.org/10.1017/CBO9781107273610).
- 24 A. Abdoulatuf, Modeling and simulation of guided waves propagation in elastic mediums in the presence of uncertainties: Application to ultrasonic characterization, *PhD*, Laboratoire Modélisation et Simulation Multi Echelle, MSME UMR 8208 CNRS, Université Paris-Est, 61, avenue du Général de Gaulle, 94010 Créteil Cedex - FRANCE, 2017.
- 25 K. Peng, C. Xu, X. Guo and D. Xiao, Detection Resolution of Acoustic Microscopy in Micro-Scale, *Appl. Mech. Mater.*, 2013, **455**, 448–454, DOI: [10.4028/www.scientific.net/AMM.455.448](https://doi.org/10.4028/www.scientific.net/AMM.455.448).
- 26 H. Yan, K. Peng, C. Xu and Q. Lin, Properties of Films Characterized by Scanning Acoustic, Microscope, *Adv. Mater. Res.*, 2013, **1061–1062**, 141–144, DOI: [10.1109/FENDT.2013.6635544](https://doi.org/10.1109/FENDT.2013.6635544).
- 27 I. K. Park and T. S. Park, Thickness Measurement of Aluminum Thin Film using Dispersion Characteristic of Surface Acoustic Wave, *Int. J. Smart Sens. Intell. Syst.*, 2014, **7**, 1–4, DOI: [10.21307/ijssis-2019-049](https://doi.org/10.21307/ijssis-2019-049).
- 28 T. Ghosh, K. I. Maslov and T. Kundu, A new method for measuring surface acoustic wave speeds by acoustic microscopes and its application in characterizing laterally inhomogeneous materials, *Ultrasonics*, 1997, **35**, 357–366, DOI: [10.1016/S0041-624X\(97\)00012-7](https://doi.org/10.1016/S0041-624X(97)00012-7).
- 29 W. Węglewski, K. Bochenek, M. Basista, T. Schubert, U. Jehring, J. Litniewski and S. Mackiewicz, Comparative assessment of Young's modulus measurements of metal–ceramic composites using mechanical and non-destructive tests and micro-CT based computational modeling, *Comput. Mater. Sci.*, 2013, **77**, 19–30, DOI: [10.1016/j.commatsci.2013.04.007](https://doi.org/10.1016/j.commatsci.2013.04.007).
- 30 S. Witkiewicz-Lukaszek, V. Gorbenko, T. Zorenko, Y. Syrotych, J. A. Mares, M. Nikl, O. Sidletskiy, P. Bilski, A. Yoshikawa and Y. Zorenko, Composite Detectors Based on Single-Crystalline Films and Single Crystals of Garnet Compounds, *Materials*, 2022, **15**, 1249, DOI: [10.3390/ma15031249](https://doi.org/10.3390/ma15031249).
- 31 K. Dynowski, J. Litniewski and A. Nowicki, Three-dimensional imaging in ultrasonic microscopy, *Arch. Acoust.*, 2014, **32**, 71–75.
- 32 G.-Y. Li, Y. Zheng, Y.-X. Jiang, Z. Zhang and Y. Cao, Guided wave elastography of layered soft tissues, *Acta Biomater.*, 2019, **84**, 293–304, DOI: [10.1016/j.actbio.2018.12.002](https://doi.org/10.1016/j.actbio.2018.12.002).
- 33 Genetic Algorithm – MATLAB & Simulink, (n.d.), <https://www.mathworks.com/help/gads/genetic-algorithm.html> (accessed April 11, 2024).
- 34 M. J. Weber, *CRC Handbook of Laser Science and Technology Supplement 2: Optical Materials*, CRC Press, Boca Raton, 2020, DOI: [10.1201/9781003067955](https://doi.org/10.1201/9781003067955).
- 35 P. D. Dragic, M. G. Pamato, V. Iordache, J. D. Bass, C. J. Kucera, M. Jones, T. W. Hawkins and J. Ballato, Athermal distributed Brillouin sensors utilizing all-glass optical fibers fabricated from rare earth garnets: LuAG, *New J. Phys.*, 2015, **18**, 015004, DOI: [10.1088/1367-2630/18/1/015004](https://doi.org/10.1088/1367-2630/18/1/015004).
- 36 Y. Fu, J. Li, C. Wang, T. Xie, W. Li, L. Wu and Y. Pan, Fabrication and properties of highly transparent Yb:LuAG ceramics, *J. Alloys Compd.*, 2016, **664**, 595–601, DOI: [10.1016/j.jallcom.2015.09.258](https://doi.org/10.1016/j.jallcom.2015.09.258).
- 37 H. Przybylińska, A. Wittlin, C.-G. Ma, M. G. Brik, A. Kamińska, P. Sybilski, Y. Zorenko, M. Nikl, V. Gorbenko, A.

- Fedorov, M. Kučera and A. Suchocki, Rare-earth antisites in lutetium aluminum garnets: Influence on lattice parameter and Ce³⁺ multicenter structure, *Opt. Mater.*, 2014, **36**, 1515–1519, DOI: [10.1016/j.optmat.2014.04.015](https://doi.org/10.1016/j.optmat.2014.04.015).
- 38 T. Kundu, J. Bereiter-Hahn and K. Hillmann, Measuring elastic properties of cells by evaluation of scanning acoustic microscopy V(Z) values using simplex algorithm, *Biophys. J.*, 1991, **59**, 1194–1207.
- 39 J. Hoffmann, S. Sathish, E. B. Shell, S. Fassbender and N. Meyendorf, Acoustic Imaging Techniques for Characterization of Corrosion, Corrosion Protective Coatings, and Surface Cracks, in *Nondestructive Materials Characterization: With Applications to Aerospace Materials*, ed. N. G. H. Meyendorf, P. B. Nagy and S. I. Rokhlin, Springer, Berlin, Heidelberg, 2004, pp. 294–322, DOI: [10.1007/978-3-662-08988-0_11](https://doi.org/10.1007/978-3-662-08988-0_11).
- 40 Z. Huang, J. Feng and W. Pan, Elastic properties of YAG: First-principles calculation and experimental investigation, *Solid State Sci.*, 2012, **14**, 1327–1332, DOI: [10.1016/j.solidstatesciences.2012.07.008](https://doi.org/10.1016/j.solidstatesciences.2012.07.008).
- 41 G. Saatsakis, D. Linardatos, G. Karpetas, N. Kalyvas, K. Ninos, A. Bakas, E. Lavdas, G. Fountos, I. Kandarakis, I. Valais and C. Michail, On the thermal response of LuAG:Ce single crystals, *Procedia Struct. Integr.*, 2021, **33**, 287–294, DOI: [10.1016/j.prostr.2021.10.035](https://doi.org/10.1016/j.prostr.2021.10.035).